Supplementary materials for "Piezochromism in the magnetic chalcogenide MnPS$_3$"

Nathan C. Harms,[1] Heung-Sik Kim,[2,3,3] Amanda J. Clune,[1] Kevin A. Smith,[1] Kenneth R. O'Neal,[1,4] Amanda V. Haglund,[5] David G. Mandrus,[5,6] Zhenxian Liu,[7] Kristjan Haule,[2] David Vanderbilt,[2] and Janice L. Musfeldt[1,8]

[1]*Department of Chemistry, University of Tennessee, Knoxville, Tennessee 37996, USA*
[2]*Department of Physics and Astronomy,*
Rutgers University, Piscataway, New Jersey 08854, USA
[3]*Department of Physics, Kangwon National University, Chuncheon 24341, Korea*
[4]*Center for Integrated Nanotechnologies,*
Los Alamos National Laboratory, Los Alamos, New Mexico 87545, USA
[5]*Department of Materials Science and Engineering,*
University of Tennessee, Knoxville, Tennessee 37996, USA
[6]*Materials Science and Technology Division,*
Oak Ridge National Laboratory, Oak Ridge, Tennessee 37831, USA
[7]*Department of Physics, University of Illinois at Chicago, Illinois 60607-7059, USA*
[8]*Department of Physics, University of Tennessee, Knoxville, Tennessee 37996, USA**

* musfeldt@utk.edu

SUPPLEMENTARY DISCUSSION

There are a number of effects that combine to make the interpretation of the Raman response challenging. First, there is a dramatic intensity reduction with increasing pressure. This trend is so striking that it is tempting to associate the decrease in mode intensity with important physics. Instead, this effect is due to to a simple shift of the band gap across the exciting laser line. In other words, green laser light is scattered (and not strongly absorbed) at low pressures whereas it is absorbed above 5 or 6 GPa because the electronic excitations of $MnPS_3$ shift into resonance. The effect is summarized in the supplement of Wang *et. al.* [S1] as well as in Supplementary Figure 1a.

To avoid overwhelming evidence for a symmetry modification with dramatic intensity changes from secondary sources, we normalize the Raman scattering spectra of $MnPS_3$ and plot this result as a function of pressure [Supplementary Figure 1b]. Within our sensitivity, there are no mode combinations in the 10 GPa range - inconsistent with a straight-forward space group modification [S2]. One interpretation of this finding is that there is no sliding transition in $MnPS_3$. But is it likely that the Mn and Fe analogs are so different? We do not believe so.
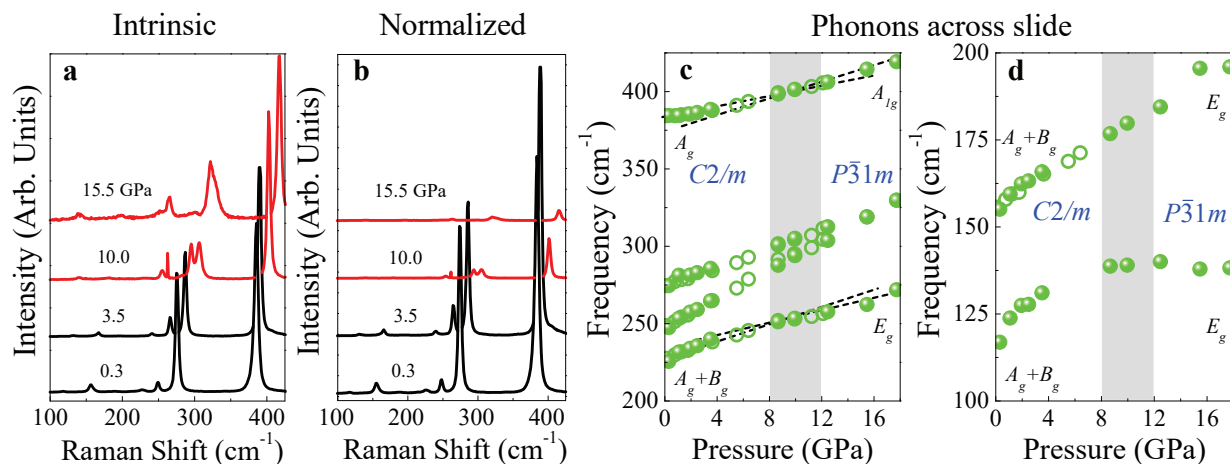
Supplementary Figure 1. Raman response across sliding transition: **a,b** Intrinsic and normalized Raman scattering response at 300 K. The spectra are offset for clarity. **c,d** Frequency vs. pressure trends for several phonons showing the subtle crossover near 10 GPa as discussed in the text. A secondary run shown with open circles is included to provide a more complete data set.

A detailed inspection reveals a much more intricate situation. It is important to recall that Raman scattering in this frequency range probes localized vibrational modes. These are intra-slab phonons that are sensitive to local structure. To these modes, a sliding transition is only a weak proximity effect. Because intra-slab phonons are not expected to be sensitive to long-range structural modifications, it is challenging to distinguish specific phonons belonging to different phases because $C2/m$ and $P\bar{3}1m$ are very similar in terms of their local symmetries. We attribute the absence of traditional signatures of a symmetry-raising transition [S2] to the inter-slab nature of the sliding [S3].
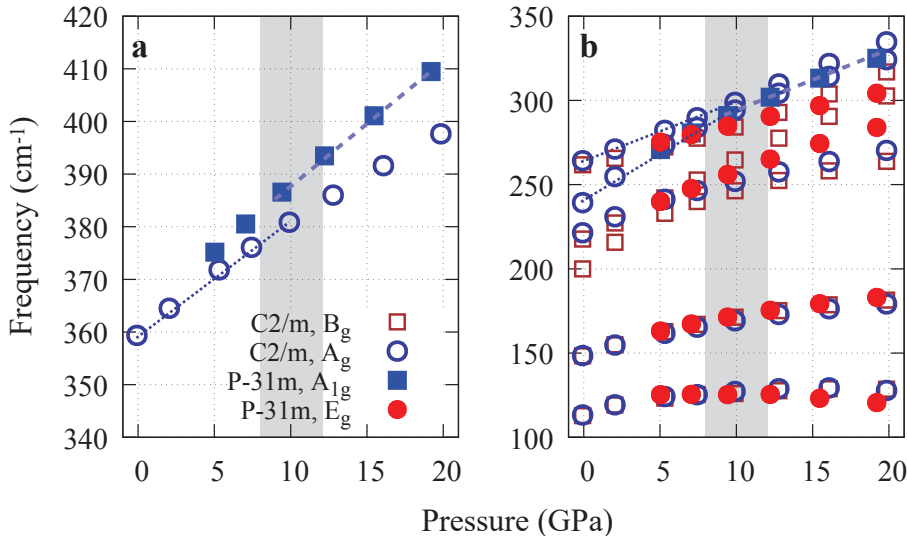
Supplementary Figure 2. Calculated frequencies of Raman-active modes: **a,b** Calculated frequencies of Raman-active modes from aligned and staggered phosphorus-dimer structures as a function of pressure where panels **a** and **b** show different frequency ranges. Dashed lines guide the eye, and the shaded areas depict the pressure range where the sliding transition is suggested to occur.

This does not mean that there is no evidence for a sliding transition in $MnPS_3$. Examination of peak position vs. pressure data [Supplementary Figure 1c] reveals trends that are subtly different from the usual expectation (which is mode hardening under compression [S4]). Here, mode frequencies harden until about 10 GPa after which they show a small change in slope. For the majority of phonons in $MnPS_3$, the change in slope is gradual and at the limit of our sensitivity. The crossover features in the phonon spectra are consistent with the proposed $C2/m$ (staggered phosphorus-dimer) to $P\bar{3}1m$ (aligned phosphorus-dimer) space group modification across the pressure-induced sliding transition. The different

$\partial\omega/\partial P$'s above 10 GPa are also in line with the development of a new phase. The 117 and 155 cm^{-1} modes are A_g+B_g symmetry features. There are multiple calculated modes close to the experimental peak frequencies, so it is not possible to assign modes to all of the peaks, although the lowest frequency mode is probably translational in nature [S5].

The gradual shift of the Raman-active mode frequencies as a function of pressure can be compared with calculated mode trends [Supplementary Figure 2]. We adopt two structural models, the staggered and aligned phosphorus-dimer models, which are suggested to be the ground states at ambient pressure and above about 5 GPa after the sliding transition, respectively. The calculated Raman-active mode trends reproduce the most distinct features in the experimental data: (i) stiffening of the feature near 390 cm^{-1}, (ii) softening of the mode near 225 cm^{-1}, and (iii) the approach of two modes near 250 cm^{-1} (see dashed and dotted lines). This agreement further supports the presence of a sliding transition in this compound. Trends of the 117 cm^{-1} feature under pressure are also in superb agreement with our simulations.

Supplementary Figure 3 summarizes our results across the pressure-driven insulator-metal transition in MnPS$_3$. The absorbance has a traditional behavior. In the insulating phase, the background is low and relatively flat - punctuated by several strong phonons. Absorbance begins to increase above 17.3 GPa, although in our hands, the P–S stretching mode is still present at 25.2 GPa [Supplementary Figure 3d]. There is a complete loss of signal at 28.2 GPa because the sample no longer transmits light. Infinite absorbance is consistent with metallicity [Supplementary Figure 3a,c]. That said, the infrared signature of the lower frequency phonons is apparent all the way up to 27.0 GPa - just below the insulator-metal transition [Supplementary Figure 4]. The frequency shifts under compression are systematic.

We also explored the development of metallicity via reflectance measurements using the diamond anvil cell [Supplementary Figure 3b,d]. In the insulating phase, the reflectance is low and flat, punctuated by a very strong P–S stretching mode at 580 cm^{-1}. The overall level begins to rise with increasing pressure, and a Drude develops at 28.2 GPa. The P–S stretching mode completely disappears because metallic carriers (evidenced by the Drude) screen the phonon.
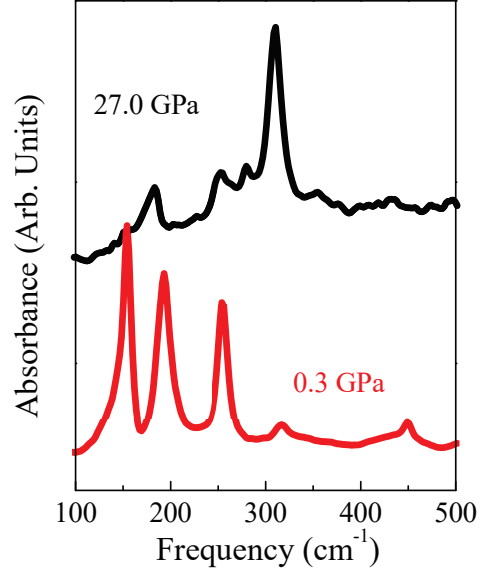
Supplementary Figure 5 shows the enthalpy difference between the aligned and staggered phosphorus-dimer phases, $\Delta H(P) \equiv H_{P\bar{3}1m}(P) - H_{C2/m}(P)$, as a function of pressure. Cal-
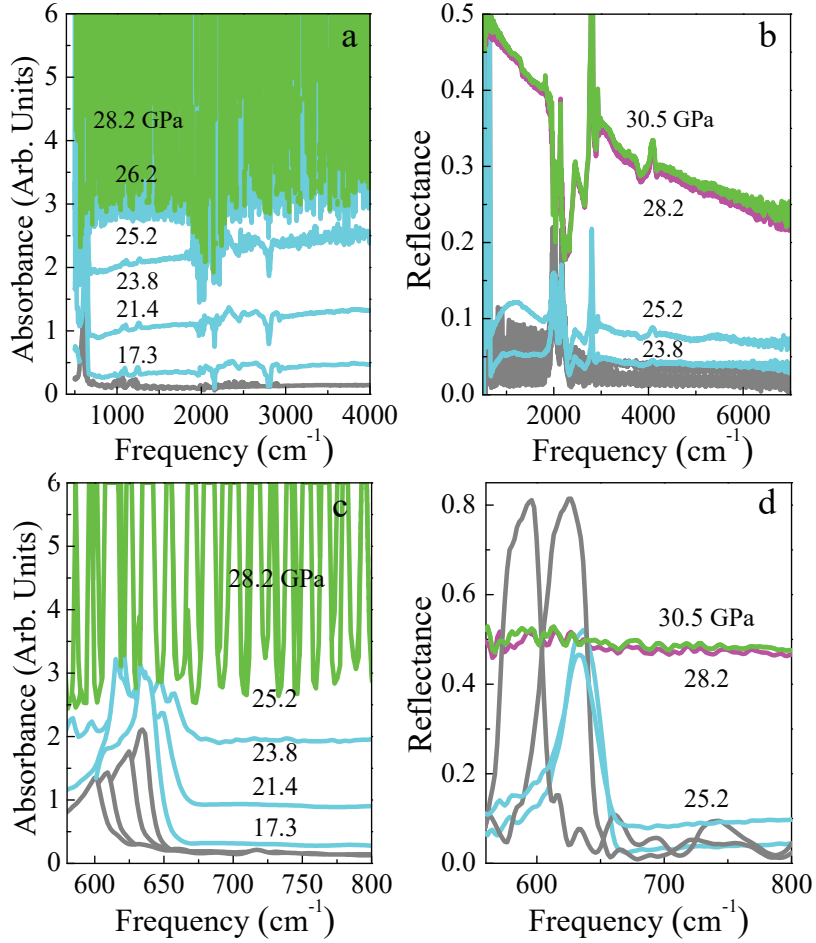
Supplementary Figure 3. Infrared response across the insulator-metal transition: **a,** Absorbance of $MnPS_3$ as a function of frequency (calculated from the measured transmittance) at various pressures. The metallic state is characterized by a loss of spectral integrity as the absorbance becomes infinite. **b,** Reflectance as a function of frequency provides evidence for the insulator-metal transition. **c,d** Close-up view of the absorbance and reflectance of $MnPS_3$ as a function of frequency showing the strong P–S stretching mode at low pressures and the sudden disappearance of this feature above the insulator-metal transition.

culations employed PBE+U_{eff} (4 eV) in addition to the optB86b van der Waals functional as implemented in VASP code (Please check the main text for relevant references). The aligned phosphorus-dimer phase become more stable beyond $P = 6$ GPa, but the actual transition pressure may vary depending on the choice of exchange-correlation van der Waals functional. Note that the enthalpy difference between the two phases is only about 10 meV per formula

5

Supplementary Figure 4. Low frequency infrared-active phonons on approach to the insulator-metal transition: Close-up view of the room temperature infrared response revealing the presence of well-defined low-frequency phonons up to the critical pressure.

unit in the pressure range of $0 < P < 10$ GPa, implying proliferation of sliding behavior and stacking faults near the critical pressure. The crossover-like behavior in the Raman spectra around 10 GPa may be attributed to this effect.

Supplementary Figure 5. Stability of aligned phosphorus-dimer phase with respect to the monoclinic staggered phosphorus-dimer phase in $MnPS_3$ as a function of pressure: Calculated enthalpy difference between the aligned and staggered phosphorus-dimer structures as a function of pressure. The aligned phosphorus-dimer structure is more stable beyond 6 GPa.
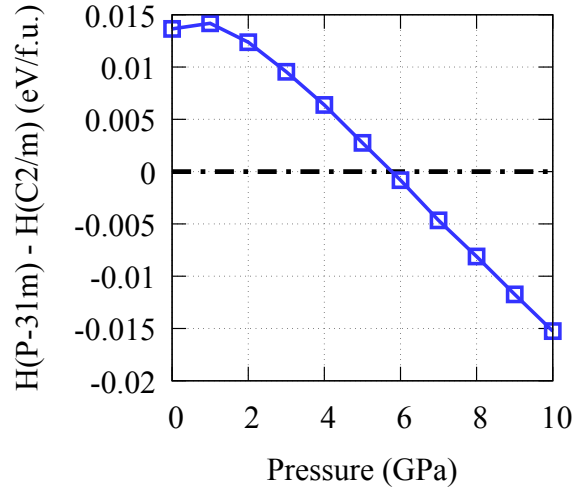
Supplementary Figure 6 shows optical conductivity $\sigma_1(E)$ of the aligned and staggered phosphorus-dimer phases from DMFT computation results. Both at ambient pressure and around $P \approx 20$ GPa the position of the onset of nonzero $\sigma_1(E)$ is almost same, unlike the charge gap which is significantly smaller for the $P\bar{3}1m$-like phase as discussed in the main text. This observation is consistent with the behavior of optical gap in the main text; because two structurally distinct phases show almost the same optical gap, the sliding

6

Supplementary Figure 6. Comparison of optical conductivity $\sigma_1(E)$ computed with two different stacking patterns: Computed optical conductivity $\sigma_1(E)$ of the aligned and staggered phosphorus-dimer structures at ambient pressure and approximately 20 GPa.
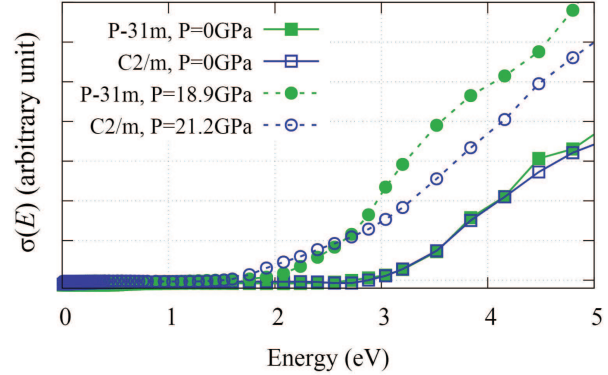
transition which happens around 6 GPa becomes invisible to an absorption measurement.

	P-dimer	P-chain
P_{PS} (GPa)	40.4	45.6
a (Å)	5.370	5.747
b (Å)	9.301	9.568
$b/\sqrt{3}a$	0.999	0.961
c (Å)	5.348	4.527
V (Å^3/f.u.)	133.5	124.5
β	90.0	90.0
Mn (4g)	(0.0000, 0.3330, 0.0000)	(0.0000, 0.3372, 0.0000)
P (4i)	(0.0001, 0.0000, 0.8036)	(-0.0007, 0.0000, 0.7583)
S1 (4i)	(0.6489, 0.0000, 0.6991)	(0.6462, 0.0000, 0.6970)
S2 (8j)	(0.1760, 0.1756, 0.6986)	(0.1802, 0.1804, 0.7094)
$d_{\mathrm{P-P}}$ (Å)	2.097, 3.251	2.186, 2.341

Supplementary Table 1. Crystal structures of the aligned P-dimer and P-chain structures before and after the metallization transition around 45 GPa, respectively. In optimizing both structures, no layer-normal three-fold symmetry is enforced. The two P–P distances (intra and interdimer distances) are shown in the last row.

Supplementary Table S1 presents detailed crystal structures of the aligned P-dimer and P-chain phases before and after the pressure-induced insulator-to-metal transition, respec-

tively, obtained via PBEsol+U_{eff} structural optimizations. The most significant difference is, as discussed in the main text, the sudden collapse of the **c** parameter and the resulting weakening of P–P dimerization. Additional feature in the metallized structure is the enhanced in-plane monoclinicity (*i.e.* $b < \sqrt{3}a$). This monoclinicity is a byproduct of the metallic character induced by the **c**-axis collapse and the weakening of phosphorus dimerization. It is not the direct cause of the metallization (*i.e.* metallization happens even with $b = \sqrt{3}a$ fixed).

From the continuous-time quantum Monte Carlo calculation results on atomic sites within the DFT+DMFT self-consistency loop, we can predict the probability of each atomic multiplets including high spin $S = 5/2$ configurations. We confirmed that, while the probability of the $S = 5/2$ states does not go below 60% up to $P = 45$ GPa in the SPD and APD phases, it suddenly collapses to approximately 20% as the transition to the APC phase occurs around 45 GPa. At the transition, both the Mn on-site charge and spin fluctuations $\delta n \equiv \sqrt{\langle n^2 \rangle - \langle n \rangle^2}$ and δS abruptly jump. This is a signature of a Mott transition from a strongly correlated phase with well-defined magnetic moments to a weakly correlated phase with no local moments. In Supplementary Figure 4d and 4e of the manuscript, the spectral functions before and after the spin-state and Mott transition are compared. Metallization can be seen from the abrupt change of the density of states at the Fermi level.

For unit cell optimizations and relaxations of initial internal coordinates in this work, we employed the Vienna *ab-initio* Simulation Package (VASP) using the projector-augmented wave (PAW) basis set [S6, S7] for the density functional theory (DFT) calculations. 340 eV of plane-wave energy cutoff and 8×6×8 Monkhorst-Pack k-grid sampling were employed. For the treatment of electron correlations within DFT, a revised Perdew-Burke-Ernzerhof exchange-correlation functional for crystalline solids (PBEsol) was employed [S8], augmented by on-site Coulomb interactions for transition-metal d-orbitals within a simplified rotationally-invariant form of the DFT+U_{eff} formalism [S9]. A 10^{-4} eV/Å force criterion was employed for structural optimizations. For test purposes, the Ceperley-Alder local density approximation [S10] and the original PBE [S11] functionals were also employed. Structural relaxations were performed in the presence of the DFT+U_{eff} (4 eV) on-site Coulomb interaction and Néel-type antiferromagnetic order [S12]. The relaxation technique was tested in Ref. S13, revealing that PBEsol+$U_{eff} = 4$ eV gives the most reasonable agreement for lattice
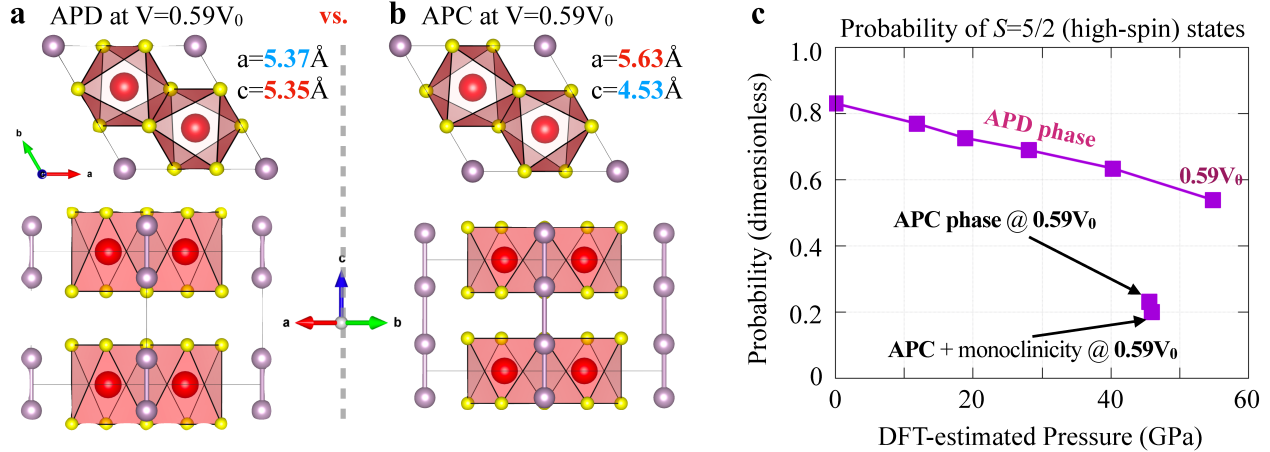
Supplementary Figure 7. Spin-state transition at the APD-APC transition: **a**, APD and **b**, APC structures at the same unit cell volume of $V = 0.59V_0$, where V_0 is the ambient-pressure volume. **c**, evolution of the $S = 5/2$ high-spin states of Mn site as a function of pressure and crystal structure. The APC + monoclinicity phase denotes the ground state of $MnPS_3$ beyond 45 GPa, where additional monoclinicity comes in due to the tendency towards intermetallic covalency between weakly correlated in-plane Mn ions.

parameters and gap sizes compared to experimentally observed values [S1]. The optB86b [S14] van der Waals functional as implemented in VASP, which showed the most reasonable results from benchmark calculations [S13], was adopted for the enthalpy comparison between the APD and SPD structures. Please refer to Ref. S13 for more information on computational details.

A fully charge-self-consistent dynamical mean-field method [S15], implemented in the DFT + Embedded DMFT (eDMFT) code, (http://hauleweb.rutgers.edu/tutorials/) combined with WIEN2K [S16], wass employed for computations of electronic properties and optimizations of internal coordinates [S17]. For DFT+DMFT calculations, we used the same computational parameters as adopted in Ref. S13.

―――――

[S1] Wang, Y. *et al.* Pressure-driven cooperative spin-crossover, large-volume collapse, and semiconductor-to-metal transition in manganese (II) honeycomb lattices. *J. Am. Chem. Soc.* **138**, 15751-15757 (2016).

[S2] Neal, S. *et al*. Near-field infrared spectroscopy of monolayer $MnPS_3$. *Phys. Rev. B* **100**, 075428 (2019).

[S3] Haines, C. *et al*. Pressure-induced electronic and structural phase evolution in the van der waals compound $FePS_3$. *Phys. Rev. Lett.* **121**, 266801 (2018).

[S4] Brinzari, T.V. *et al*. Local lattice distortions in $Mn[N(CN)_2]_2$ under pressure. *Inorg. Chem.* **55**, 1956-1961 (2016).

[S5] Mathey, Y., Clement, R., Sourisseau, C. & Lucazeau, G. Vibrational study of layered MPX_3 compounds and of some intercalates with $Co(\eta^5\text{-}C_5H_5)_2^+$ or $Cr(\eta^6\text{-}C_6H_6)_2^+$. *Inorg. Chem.* **19**, 2773-2779 (1980).

[S6] Kresse, G. & Hafner, J. Ab-initio molecular dynamics for liquid metals. *Phys. Rev. B* **47**, 558–561 (1993).

[S7] Kresse, G. & Furthmüller J. Efficient iterative schemes for ab initio total-energy calculations using a plane-wave basis set. *Phys. Rev. B* **54**, 11169–11186 (1996).

[S8] Perdew, J.P. *et al.* Restoring the density-gradient expansion for exchange in solids and surfaces. *Phys. Rev. Lett.* **100**, 136406 (2008).

[S9] Dudarev, S. L. *et al.* Electron-energy-loss spectra and the structural stability of nickel oxide: An LSDA+U study. *Phys. Rev. B* **57**, 1505–1509 (1998).

[S10] Ceperleym D. M. & Alder, B. J. Ground state of the electron gas by a stochastic method. *Phys. Rev. Lett.* **45**, 566–569 (1980).

[S11] Perdew, J.P., Burke, K., & Ernzerhof, M. Generalized gradient approximation made simple. *Phys. Rev. Lett.* **77**, 3865–3868 (1996).

[S12] Brec, Raymond. Review on structural and chemical properties of transition metal phosphorous trisulfides MPS_3. *Solid State Ion.* **22**, 3 – 30 (1986).

[S13] Kim, H. S., Haule, K. & Vanderbilt, D. Mott metal-insulator transitions in pressurized layered trichalcogenides. *Phys. Rev. Lett.* **123**, 236401 (2019).

[S14] Klimeš, J., Bowler, D.R. & Michaelides, A. Chemical accuracy for the van der waals density functional. *J. Phys. Condens. Matter* **22**, 022201 (2009).

[S15] Haule, K., Yee, C-H. & Kim, Kyoo. Dynamical mean-field theory within the full-potential methods: Electronic structure of $CeIrIn_5$, $CeCoIn_5$, and $CeRhIn_5$. *Phys. Rev. B* **81**, 195107 (2010).

[S16] Blaha, K. *et al.* An augmented plane wave + local orbitals program for calculating crystal properties (Karlheinz Schwarz, Techn. Universität Wien, Austria, 2001).

[S17] Haule, Kristjan & Pascut, Gheorghe L. Forces for structural optimizations in correlated materials within a DFT+embedded DMFT functional approach. *Phys. Rev. B* **94**, 195146 (2016).